GEOPHYSICAL RESEARCH LETTERS, VOL. 33, L13803, doi:10.1029/2006GL026350, 2006

Validation of rainfall estimates from the TRMM precipitation radar and microwave imager using a radiative transfer model: 1. Comparison of the version-5 and -6 products

S. Shige,[1] H. Sasaki,[1] K. Okamoto,[1] and T. Iguchi[2]

Received 20 March 2006; revised 8 May 2006; accepted 24 May 2006; published 6 July 2006.

[1] The Tropical Rainfall Measuring Mission (TRMM) version-6 rainfall products show the reduced bias between Precipitation Radar (PR) and TRMM Microwave Imager (TMI) rainfall estimates during the 1997/1998 El Niño event noted in version 5, but need to be verified. We investigate consistency between TMI-observed brightness temperatures (TBs) at 10 and 19 GHz channels and those simulated from the PR and TMI rainfall estimates using a radiative transfer model. Simulated TBs from PR V6 exhibits better agreement with observed ones than those from PR V5, implying the algorithm improvements. However, discrepancies at 19 GHz suggest that uncertainty in the assumed drop size distribution still remains in PR V6. Simulated TBs from TMI V6 also exhibits better agreement with observed ones than those from TMI V5. However, the simulated 10-GHz TBs from TMI V6 exhibits more scatter against TMI-observed ones than those from PR V6 do. **Citation:** Shige, S., H. Sasaki, K. Okamoto, and T. Iguchi (2006), Validation of rainfall estimates from the TRMM precipitation radar and microwave imager using a radiative transfer model: 1. Comparison of the version-5 and -6 products, *Geophys. Res. Lett.*, *33*, L13803, doi:10.1029/2006GL026350.

1. Introduction

[2] The Tropical Rainfall Measuring Mission (TRMM) satellite has been in operation for more than 8 years, providing the distribution of rainfall throughout the Tropics using microwave observations from the Precipitation Radar (PR) and the TRMM Microwave Imager (TMI). The PR is the first space-borne precipitation radar and can provide height information based upon the time delay of the precipitation-backscattered return power. This allows us for vertical profiles of precipitation to be obtained directly over the global Tropics. On the other hand, the TMI measures radiances that are the end product of the integrated effects of electromagnetic absorption/emission and scattering through a precipitating cloud along the sensor viewpath. Comparisons of tropical mean rainfall time series indicate that there are large discrepancies between the TRMM version-5 rainfall products derived by the PR (2A25) and TMI (2A12) profiling algorithms during the 1997/1998 El Niño (warm) event [*Robertson et al.*, 2003].

[3] Several improvements have been implemented to create the most recent algorithm, the TRMM version 6 algorithms. The TRMM version-6 rainfall products show the reduced bias during the warm event, but need to be verified. The most common method of verifying satellite-retrieved rain estimates is to directly compare to ground validation measurements (ground truth) derived from rain gauge networks, ground weather radar, or a combination of the two. *Wolff et al.* [2005] showed satellite retrievals from the V6 of TMI, PR, and Combined algorithms are well agree within 10% of TRMM Ground Validation (GV) estimates at the Kwajalein site, which is located on the eastern boundary of western Pacific warm pool. *Yang et al.* [2006] also compared TMI V6 estimates to TRMM GV estimates at the Kwajalein site, as well as PR V5 and TMI V5 estimates. However, during the El Niño event, larger discrepancies between the TRMM estimates are found over eastern Pacific where there are no TRMM GV sites. Thus, we must rely on indirect strategies to achieve validation. *Viltard et al.* [2000] investigated the consistency in TMI-observed brightness temperatures (hereinafter TBs) and those simulated from PR2A25 V4 rain profiles for a case in the central Pacific. In this paper, the consistency between TMI-observed TBs at lower frequency channels (10.7 and 19.4 GHz) and those simulated from PR2A25 V5 and V6 rain profiles for the intertropical convergence zone (ITCZ) precipitation systems during the 1997/1998 El Niño event is statistically investigated using a radiative transfer model. Although this study lays weight on validation of PR2A25 using independent TMI data, the consistency between TMI-observed TBs and those simulated from TMI2A12 V5 and V6 rain profiles are also investigated to see their performance.

2. Approach

[4] Figure 1 shows the schematic flow diagram of PR2A25 and TMI2A12 algorithms and the procedure for validating the TRMM rainfall products.

[5] The PR operates at a single frequency (13.8 GHz) so that PR2A25 algorithm corrects the attenuation in the measured radar reflectivity factor Z_m and estimates the effective radar reflectivity factor Z_e [*Iguchi et al.*, 2000]. The attenuation correction is based on a hybrid of the Hitschfeld–Bordan (H-B) solution and the surface reference technique (SRT). The coefficient α in the k-Z_e relationship $k = \alpha Z_e^{\beta}$ is adjusted in such a way that the path-integrated attenuation (PIA) estimated from the H-B solution matches the SRT estimate of PIA where k is the specific attenuation due to precipitation. Major improvements in V6 are as follows: a) Inclusion of the effects of attenuation due to

[1]Department of Aerospace Engineering, Osaka Prefecture University, Osaka, Japan.
[2]National Institute of Information and Communications Technology, Tokyo, Japan.

0094-8276/06/2006GL026350$05.00

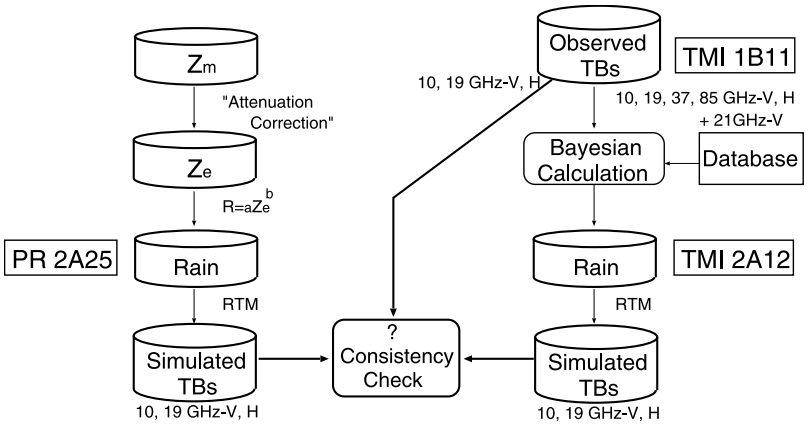

Figure 1. Diagram showing the schematic flow diagram of PR2A25 and TMI2A12 algorithms and the procedure for validating the TRMM rainfall products. The question mark means to examine consistency between TMI-observed brightness temperatures (TBs) and those simulated from the TRMM rainfall products.

cloud liquid water, water vapor, and molecular oxygen in the attenuation algorithm, b) Estimation of the attenuation between the lowest range bin that is free from the mainlobe surface clutter and the actual surface by assuming a constant slope of dBZ_e, c) Estimation of Z_e, rain and several parameters that varies with the adjustment parameter (ϵ) of α as the expected values with respect to the posterior probability distribution function of ϵ, d) Reevaluation of the error estimate in the PIA by the SRT and that from the H-B solution. See the detailed descriptions by Iguchi et al. (manuscript in preparation, 2006) on improvements made on 2A25 V6.

[6] On the other hand, the basis of TMI 2A12 algorithm is on a Bayesian framework, in which retrieved precipitation are constructed from those cloud-resolving model (CRM)-generated profiles that are radiatively consistent with the observation [*Kummerow and Coauthors*, 2001]. Major improvements in V6 are: a) Greater diversity in the supporting cloud-radiative model database, b) Adjustment of CRM ice microphysics, c) Inclusion of the effects of mixed-phase precipitation in CRM simulations, d) Definition of cloud and precipitation properties in simulated footprints, e) New geographic database, f) Calculation of the ''background'' rain-free radiance field, g) Reformulation of the convective/non-convective rain area constraint. See the detailed descriptions by *Olson et al.* [2006] and *Yang et al.* [2006] on improvements made on 2A12 V6.

[7] Due to the scarcity of reliable validation data and difficulties associated with the collocation of validation data and satellite measurements, we investigate the consistency in observed and simulated TBs. Here, the simulated TBs are derived from PR2A25 and TMI2A12 rain profiles. In this study, we focus on lower-frequency channels (10.7 GHz and 19.4 GHz). This is because lower-frequency brightness temperatures are well correlated with total liquid water path and because less uncertainties in approximative radiative transfer at lower-frequency channels are expected than at higher-frequency channels (37 GHz and 85.5 GHz) where scattering by ice-phase precipitation is significant.

[8] The radiative transfer model (RTM) developed by *Liu* [1998] is used to calculate TBs. All radiance slant paths through the three-dimensional domain are considered independently. The antenna pattern for each frequency is approximated by a Gaussian weighting function with the same 3-dB beamwidth as the actual antenna pattern.

[9] The upwelling microwave radiances over ocean depend on the sea surface characteristics and atmospheric constitutes. In this study, mean atmospheric temperature from the 6-hourly ERA40 reanalysis data with minimum time difference with the TRMM observations are employed. The column water vapor (CWV), liquid water path (LWP), sea surface wind, and sea surface temperature are adopted from the TMI products provided by Remote Sensing Systems. The water vapor profiles are determined from CWV, following *Masunaga and Kummerow* [2005]. Our simulated TBs in clear-air areas show very good agreement with TMI measurements. For TBs simulations from PR2A25 estimates, the cloud water profiles in nonraining areas are determined from LWP, following Masunaga and Kummerow. In raining areas, we used the cloud water profiles from CRM simulations based on which the PR2A25 V6 algorithm estimates the attenuation by cloud water. We utilized two drop size distribution (DSD) models of a gamma distribution corresponding to convective and stratiform rain assumed in PR algorithm (T. Kozu et al., Estimation of rain drop size distribution parameters using statistical relations between multiparameter rainfall remote sensing data, preprints of 29th International Conference on Radar Meteorology, 1999). A change in the DSD due to alternations in α accommodating the SRT estimate of PIA is also taken into account. For PR stratiform rain profiles with a bright band, *Klaassen's* [1990] melting-layer parameterization is used, following *Kim et al.* [2004]. For TBs simulations from TMI2A12 estimates, we used cloud estimates present in the TMI2A12 and the Marshall–Palmer distribution assumed in CRMs that make up the cloud-radiative model database.

[10] For comparisons, the emission index (*EI*) is defined as $1 - P$ and used instead of brightness temperature to isolate the microwave signal due to precipitation particles. Here, P is the normalized polarization difference [*Petty*, 1994] given by

$$P = \frac{TB_V - TB_H}{TB_{V,clear} - TB_{H,clear}}, \quad (1)$$

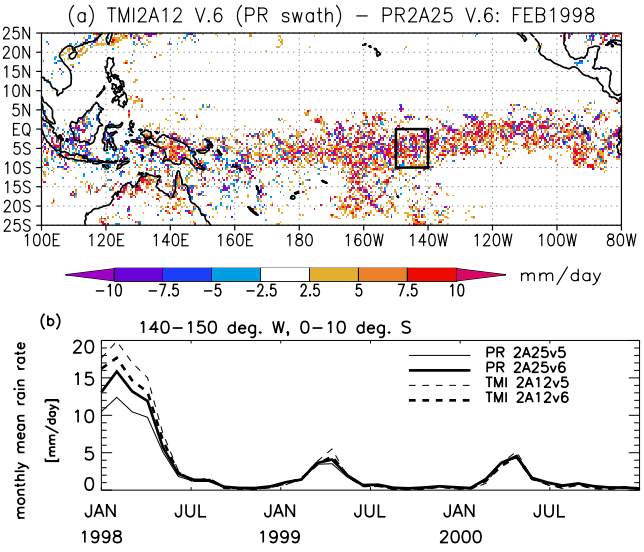

Figure 2. (a) Differences of rainfall estimates (mm day^{-1}) between PR2A25 V6 and TMI2A12 V6 for February of 1998; (b) Time series of monthly mean rainfall estimates (mm day^{-1}) from PR2A25 and TMI2A12 for the selected area extending from 0° to 10°S latitude and from 140° to 150°W longitude indicated by a box in Figure 2a. Only TMI data matched within PR swath are used.

where TB_V and TB_H are the vertically and horizontally polarized brightness temperatures and $TB_{V,clear}$ and $TB_{H,clear}$ are background brightness temperatures in the absence of cloud and/or precipitation. For the observed P, the back ground brightness temperatures are estimated following the method of TMI 2A12 V6 [*Olson et al.*, 2006]. For the simulated P, the back ground brightness temperatures are calculated with all cloud and precipitation water contents set to zero. The EI is 0 for 0 rain rate and increases with the rain rate.

3. Results and Discussions

[11] Figure 2a indicates that rainfall for February 1998 estimated by PR2A25 V6 is smaller than that estimated by TMI2A12 V6 over a well-defined ITCZ (associated with heavy rainfall) which is present in the central and eastern Pacific between the equator and 10°S. It is nevertheless obvious from Figure 2b that the difference between TMI and PR estimates for February 1998 is drastically narrowing in V6 (1.8 mm day^{-1}, or 11%) compared with V5 (7.5 mm day^{-1}, or 46%) for the area from 0° to 10°S latitude and from 140° to 150°W longtitude where larger differences are found in Figure 2a. The procedures described in the previous section are applied to 6 months of TRMM data, from January to June 1998, over this selected area. The number of TRMM orbits used in this study is 129. Only the TMI footprints for each channels of which 80% are coverd with PR rain pixels are analyzed.

[12] Frequency plots of the 10-GHz EIs (hereafter EI10s) simulated from PR2A25 V5 and V6 rain profiles against corresponding TMI-observed EI10s are presented in Figures 3a and 3b, respectively. The EI10s simulated from PR2A25 V5 are much lower than the observed EI10s, especially for the higher range (associated with heavy rainfall). This indicates that PR2A25 V5 underestimates rainfall in the ITCZ. The simulated EI10s from PR2A25 V6 are higher than those from PR2A25 V5, and exhibit better agreement with observed EI10s, especially for higher values. This is explained by the inclusion of attenuation corrections for water vapor and cloud liquid water. A more relative weight to the SRT PIA in V6 than V5 due to changing of the weighting factors between the PIA estimated by the SRT and that by H-B solution also accounts for the better agreement in V6 than V5.

[13] Frequency plots of the EI10s simulated from TMI2A12 V5 and V6 rain profiles against corresponding TMI-observed EI10s are presented in Figures 3c and 3d, respectively. The EI10s simulated from TMI2A12 V5 are higher than the observed EI10s, especially for the higher range (associated with heavy rainfall). This indicates that TMI2A12 V5 overestimates rainfall in the ITCZ. Thus, both PR2A25 and TMI2A12 algorithms account for the inconsistencies in the TRMM V5 rainfall products. The simulated EI10s from TMI2A12 V6 are lower than those from TMI2A12 V5, and exhibit better agreement with observed EI10s for higher values. *Yang et al.* [2006] attributed the reduced high bias in TMI2A12 V6 to the expanded cloud-radiative model database supporting the V6 algorithm, as well as the more consistent and specific convective/stratiform rain separation procedure, which together reduce the high bias in estimated stratiform rains previously noted in

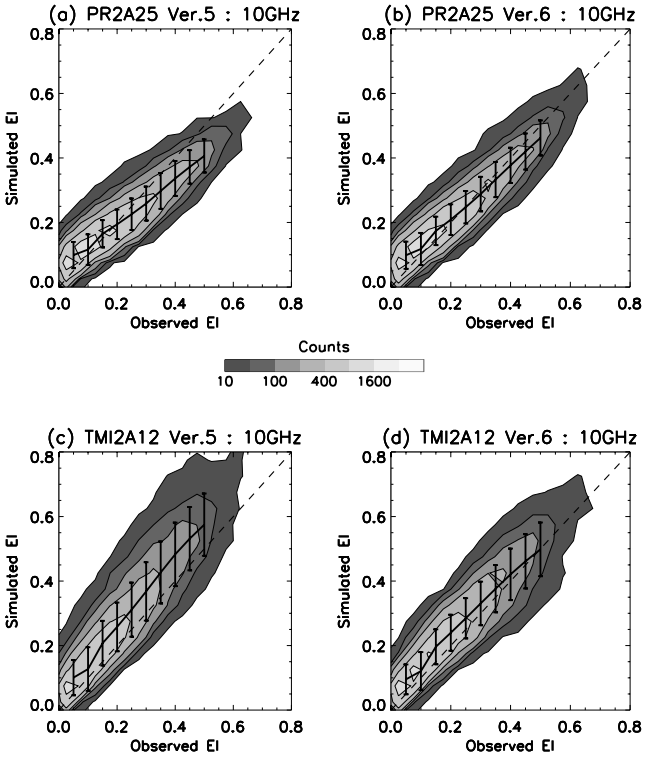

Figure 3. Frequency plots of the 10-GHz emission indexes (EIs) simulated from (a) PR2A25 V5, (b) PR2A25 V6, (c) TMI2A12 V5, and (d) TMI2A12 V6 rain profiles against corresponding TMI-observed 10-GHz EIs. The average (solid line) and standard deviation (error bars) of simulated EI for each histogram bin along the horizontal line are plotted. The dashed lines are the 1:1 lines.

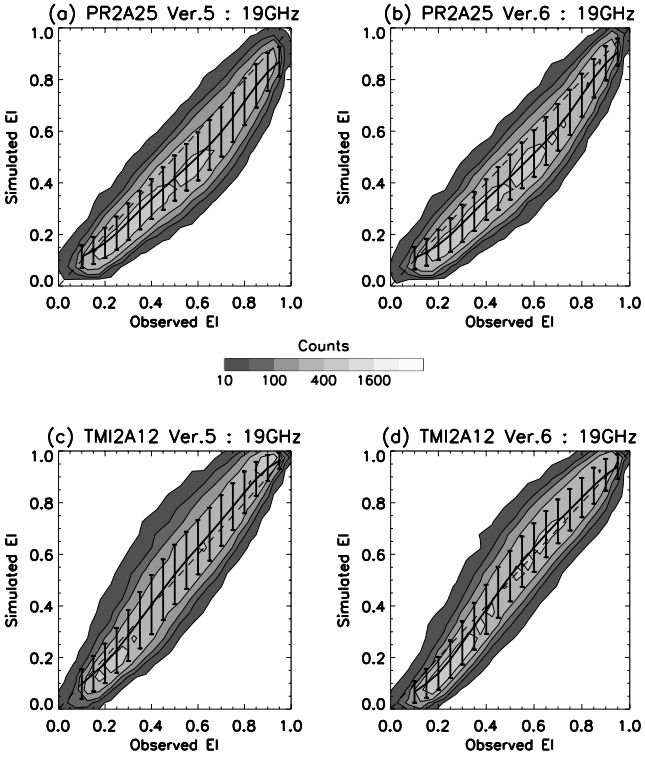

Figure 4. Same as Figure 3 except for the 19-GHz *EI*s simulated from (a) PR2A25 V5, (b) PR2A25 V6, (c) TMI2A12 V5, and (d) TMI2A12 V6 rain profiles against corresponding TMI-observed 19-GHz *EI*s.

V5. These improvements may account for the better agreement in V6 than V5. On the other hand, the scatter of the simulated *EI*10s from TMI2A12 V6 increases as the observed *EI*10s. Although the 10 GHz channel is used in TMI2A12 but not in PR2A25, the scatter of the simulated *EI*10s from TMI2A12 V6 is higher than that of the simulated *EI*10s from PR2A25 V6 (Figures 3b and 3d). This indicates that the 10 GHz channel does not make significant contribution in TMI2A12 because of their low resolution. Although the footprint of 10 GHz channel is very large, this channel provides total liquid water path estimates and avoids saturation from such heavy rainfall. Thus, the 10 GHz channel may be very important, although the information from it is underused in the current TMI2A12.

[14] Frequency plots of the 19-GHz *EI*s (hereafter *EI*19s) simulated from PR2A25 V5 and V6 rain profiles against corresponding TMI-observed *EI*19s are presented in Figures 4a and 4b, respectively. The simulated *EI*19s from PR2A25 V6 are somewhat higher than those from PR2A25 V5, especially for the higher range. However, the simulated *EI*19s from PR2A25 V6 remain lower than the observed ones, implying underestimation of rain. For example, the simulated *EI*19 from PR2A25 V6 is about 0.4 for the observed *EI*19 of 0.5.

[15] The RTM calculations assuming horizontally uniform rain with a 5 km-depth show that *EI*19s of 0.4 and 0.5 imply rain rates of about 3 and 4 mm hr^{-1}, respectively. Since absorption of microwaves by liquid cloud and rain increases with frequency, the water content for which TB saturates is lower than for 19 GHz than for 10 GHz. Thus, comparing radiative characteristics of 19 GHz implies validating weaker rain. When attenuation is small or marginal (i.e., weaker rainrate), the weight is shifted toward the PIA estimate from the H-B solution in PR2A25. In such a case, the SRT perturbs the initial DSD model only slightly, and an appropriate selection of the initial DSD model is very important. Therefore, less agreement between TMI-observed *EI*s and those simulated from PR2A25 at 19 GHz than 10 GHz is attributed to inappropriate selection of the initial DSD model used in PR2A25 V6 that remains the same as in PR2A25 V5.

[16] In contrast to PR2A25, the simulated *EI*19s from TMI2A12 V6 rain profiles are good agreement with TMI-observed ones as well as those from TMI2A12 V5 (Figures 4c and 4d). The simulated *EI*19s from TMI2A12 V6 exhibit less scatter against TMI-observed ones than those from TMI2A12 V5 do. It is also noticed that the *EI*19s simulated from TMI2A12 V6 exhibit less scatter against TMI-observed ones than the *EI*10s simulated from TMI2A12 V6 do. This indicates that the 19 GHz channel makes more significant contribution in TMI2A12 than the 10 GHz channel because of their higher resolution.

4. Summary and Conclusion

[17] In this study, we have shown that simulated *EI*10s from PR2A25 V6 rain profiles exhibit better agreement with TMI-observed *EI*10s than those from PR2A25 V5 rain profiles during the 1997/1998 El Niño event. This is explained by the inclusion of attenuation corrections for water vapor and cloud liquid water, and a more relative weight to the SRT PIA in V6 than V5. The simulated *EI*10s from TMI2A12 V6 also exhibit better agreement with observed one than those from TMI2A12 V5. However, the simulated *EI*10s from TMI2A12 V6 exhibit more scatter against TMI-observed ones than those from PR2A25 V6 do, implying that the 10 GHz channel does not make significant contribution in TMI2A12. On the other hand, the simulated *EI*19 from PR2A25 V6, as well as from PR 2A25 V5, are lower than the observed one. This is attributed to inappropriate selection of the initial DSD model in PR2A25.

[18] Only precipitation systems over the central Pacific during the 1997/1998 El Niño event was considered in the current investigation. This study will be extended to examine regional and seasonal biases that exist between the PR2A25 V6 and TMI2A12 V6 algorithms.

[19] **Acknowledgments.** This study is supported by the fund of Japan Science and Technology Corporation - Core Research for Evolution Science and Technology (CREST). We wish to thank G. Liu of Florida State University for providing his radiative transfer model. We also thank K. Aonashi of Meteorological Research Institute for his kind guidance on using the radiative transfer model. Discussions with N. Takahashi of NICT and T. Kozu of Shimane University were appreciated. We also thank C. Kummerow for providing the TMI 2A12 V6 algorithm code. The TRMM products were provided by Japan Aerospace Exploration Agency (JAXA). ERA40 data was provided from the European Center for Medium-range Weather Forecasts (ECMWF). The CWV, LWP, sea surface wind, and sea surface temperature data set retrieved from TMI was obtained from the Remote Sensing Systems Web site.

References

Iguchi, T., T. Kozu, R. Meneghini, J. Awaka, and K. Okamoto (2000), Rain-profiling algorithm for the TRMM precipitation radar, *J. Appl. Meteorol.*, *39*, 2038–2052.

Kim, M.-J., J. A. Weinman, and R. A. Houze Jr. (2004), Validation of maritime rainfall retrievals from the TRMM microwave radiometer, *J. Appl. Meteorol.*, *43*, 847–859.

Klaassen, W. (1990), Attenuation and reflection of radio waves by a melting layer of precipitation, *IEEE Conf. Publ.*, *137*(H1), 39–44.

Kummerow, C., et al. (2001), The evolution of the Goddard profiling algorithm (GPROF) for rainfall estimation from passive microwave sensors, *J. Appl. Meteorol.*, *40*, 1801–1820.

Liu, G. (1998), A fast and accurate model for microwave radiance calculations, *J. Meteorol. Soc. Jpn.*, *76*, 335–343.

Masunaga, H., and C. D. Kummerow (2005), Combined radar and radiometer analysis of precipitation profiles for a parametric retrieval algorithm, *J. Atmos. Oceanic Technol.*, *22*, 909–929.

Olson, W. S., et al. (2006), Precipitation and latent heating distributions from satellite passive microwave radiometry. part I: Improved method and uncertainties, *J. Appl. Meteorol. Climatol.*, *45*, 702–720.

Petty, G. W. (1994), Physical retrievals of over-ocean rain rate from multichannel microwave imagery. part I: Theoretical characteristics of normalized polarization and scattering indices, *Meteorol. Atmos. Phys.*, *54*, 79–99.

Robertson, F. R., D. E. Fitzjarrald, and C. D. Kummerow (2003), Effects of uncertainty in TRMM precipitation radar path integrated attenuation on interannual variations of tropical oceanic rainfall, *Geophys. Res. Lett.*, *30*(4), 1180, doi:10.1029/2002GL016416.

Viltard, N., C. Kummerow, W. S. Olson, and Y. Hong (2000), Combined use of the radar and radiometer of TRMM to estimate the influence of drop size distribution on rain retrievals, *J. Appl. Meteorol.*, *39*, 2103–2114.

Wolff, D. B., et al. (2005), Ground validation for the Tropical Rainfall Measuring Mission (TRMM), *J. Atmos. Oceanic Technol.*, *22*, 365–380.

Yang, S., W. Olson, J. J. Wang, T. L. Bell, E. A. Smith, and C. D. Kummerow (2006), Precipitation and latent heating distributions from satellite passive microwave radiometry. part II: Evaluation of estimates using independent data, *J. Appl. Meteorol. Climatol.*, *45*, 721–739.

T. Iguchi, National Institute of Information and Communications Technology, 4-2-1 Nukui-Kitamachi, Tokyo 184-8795, Japan.

S. Shige, H. Sasaki, and K. Okamoto, Department of Aerospace Engineering, Osaka Prefecture University, 1-1 Gakuen-cho, Osaka 599-8531, Japan. (shige@aero.osakafu-u.ac.jp)